

The Crust of the Moon as Seen by GRAIL

M. A. Wieczorek,^{1*} G. A. Neumann,² F. Nimmo,³ W. S. Kiefer,⁴
G. J. Taylor,⁵ H. J. Melosh,⁶ R. J. Phillips,⁷ S. C. Solomon,⁸
J. C. Andrews-Hanna,⁹ S. W. Asmar,¹⁰ A. S. Konopliv,¹⁰ F. G. Lemoine,²
D. E. Smith,¹¹ M. M. Watkins,¹⁰ J. G. Williams,¹⁰ M. T. Zuber¹¹

¹Institut de Physique du Globe de Paris, Univ Paris Diderot,
Case 7011, Bâtiment Lamarek A, 5, rue Thomas Mann, 75205 Paris Cedex 13, France.

²Solar System Exploration Division, NASA/Goddard Space Flight Center,
Greenbelt, MD 20771, USA.

³Department of Earth and Planetary Sciences, University of California, Santa Cruz,
1156 High Street, Santa Cruz, California 95064, USA.

⁴Lunar and Planetary Institute, Houston, Texas, USA.

⁵Hawaii Institute of Geophysics and Planetology, University of Hawaii, Honolulu, HI 96822, USA.

⁶Department of Earth and Atmospheric Sciences, Purdue University,
550 Stadium Mall Drive, West Lafayette, Indiana 47907, USA.

⁷Planetary Science Directorate, Southwest Research Institute, Boulder, CO 80302, USA.

⁸Lamont-Doherty Earth Observatory, Columbia University, Palisades, NY 10964 USA.

⁹Department of Geophysics, Colorado School of Mines, 1500 Illinois St.,
Golden, CO 80401-1887 USA.

¹⁰Jet Propulsion Laboratory, Pasadena, CA 91109 USA.

¹¹Department of Earth, Atmospheric and Planetary Sciences,
Massachusetts Institute of Technology, Cambridge, MA 02139-4307, USA.

*To whom correspondence should be addressed; E-mail: wieczor@ipgp.fr

High resolution gravity data obtained from the dual GRAIL spacecraft are providing an unprecedented view of the Moon's crust. The bulk density of the highlands crust is found to be 2550 kg m^{-3} , significantly lower than generally assumed, and when combined with remote sensing and sample data, an average crustal porosity of 12% to depths of at least a few km is required. Lateral variations in crustal porosity correlate with the largest impact basins, whereas lateral variations in crustal density correlate with crustal composition. The low bulk crustal density allows construction of a global crustal thickness model that satisfies the Apollo seismic constraints, and with an average crustal thickness between 34 and 43 km, the bulk refractory element composition of the Moon is not required to be enriched with respect to Earth. [132 words]

The crust of the Moon plays an integral role in deciphering its origin and subsequent evolution. Being composed largely of anorthositic materials [1], its average thickness is key to determining the bulk silicate composition [2], and by consequence, whether the Moon is derived from Earth materials or from the giant impactor that is believed to have formed the Earth-Moon system [3]. Following formation, the crust of the Moon suffered the consequences of 4.5 billion years of impact cratering. The Moon is the nearest and most accessible planetary body to study the largest of these catastrophic events that were common during early solar system evolution [4,5]. In addition, it is an ideal laboratory for investigating the cumulative effects of the more numerous smaller events. Spatial variations in the Moon's gravity field are reflective of subsurface density variations, and GRAIL's high resolution measurements are particularly useful for investigating the crust.

Previous investigations of the Moon have made use of gravity data derived from radio tracking of orbiting spacecraft, but these studies were frustrated by the low and uneven spatial resolution of the available gravity models [6,7]. NASA's Gravity Recovery and Interior Laboratory (GRAIL) mission [8] consists of two co-orbiting spacecraft that are obtaining high-resolution

gravity measurements by intersatellite ranging over both the near and far side hemispheres of Earth’s natural satellite. Gravity models at the end of the primary mission resolve wavelengths as fine as 26 km, which is more than 4 times smaller than any previous global model. The mass anomalies associated with the Moon’s surface topography are one of the most prominent signals seen by GRAIL [9], and as the measured gravity signal at short wavelengths is not affected by the compensating effects of lithospheric flexure, these data offer the first opportunity to determine unambiguously the bulk density of the lunar crust. The density of the crust is a fundamental property required for geophysical studies of the Moon, but also provides important information on crustal composition over depth scales that are greater than those of most other remote sensing techniques.

The deflection of the crust-mantle interface to surface loads makes only a negligible contribution to the observed gravity field beyond spherical harmonic degree 150 (supporting online materials). At these wavelengths, if the gravitational contribution of the surface relief were removed with the correct reduction density, the remaining signal (the Bouguer anomaly) would be zero if there were no other density anomalies present in the crust. An estimate of the crustal density can be obtained by minimizing the correlation coefficient of the surface topography and Bouguer anomaly. To neglect complicating flexural signals, and to interpret only that portion of the gravity field that is well resolved, the gravity and topography were first filtered to include spherical harmonic degrees between 150 and 310. Gravity and topography over the high density mare basalts are excluded from analysis, as their presence would bias the bulk density determination given their preference to pool in low-lying regions.

For our analyses, the correlation coefficient of the Bouguer gravity and surface topography was minimized using data within circles that span 12° of latitude. Analyses were excluded when more than 5% of the region was covered by mare basalts, and when the minimum correlation coefficient exceeded the 95% confidence limit as estimated from Monte Carlo simulations and

the gravity coefficient uncertainties (supporting online materials). The average density of the entire highlands crust is found to be 2550 kg m^{-3} , and individual density uncertainties are on average 18 kg m^{-3} . As shown in Fig. 1, significant lateral variations in crustal density exist with amplitudes of $\pm 250 \text{ kg m}^{-3}$. The largest positive excursions are associated with the 2000-km diameter South Pole-Aitken basin on the Moon's farside hemisphere, which is a region that has been shown by remote sensing data to be composed of rocks that are considerably more mafic, and thus denser, than the surrounding anorthositic highlands [10]. Extensive regions with densities lower than average are found surrounding the impact basins Orientale and Moscoviense, which are the two largest young impact basins on the Moon's farside hemisphere. The bulk density determinations are robust to changes in size of the analysis region by a factor of two, and are robust to changes in the filter limits by more than ± 50 degrees. Nearly identical bulk densities are obtained using a localized spectral admittance approach (Fig. S6).

The bulk crustal densities obtained from GRAIL are considerably lower than the values of 2800 to 2900 kg m^{-3} that are used typically for anorthositic crustal materials [11]. We attribute the low densities to impact-induced fractures, and quantify the total porosity by use of independent estimates of crustal grain density. Using an empirical relation between the grain density of lunar rocks and their concentration of FeO and TiO_2 [12], along with surface elemental abundances derived from gamma-ray spectroscopy [13], grain densities of lunar surface materials are estimated globally with a precision and spatial resolution that is comparable to the GRAIL bulk density measurements (Fig. S3). Assuming that the surface composition of the Moon is representative of the underlying crust, the porosity of the upper levels of the highlands crust is on average 12% and varies regionally from about 4 to 21% (Fig. 2). These values are consistent with, though somewhat larger than, Kaguya-based estimates made using longer wavelengths and a lithospheric flexure model [12]. The crustal porosities in the interiors of many impact basins are lower than their surroundings, consistent with a reduction in pore space by high post-

impact temperatures that can exceed the solidus. In contrast, the porosities just exterior to many basins are higher than their surroundings, which is consistent with the generation of fractures by the ballistic deposition of impact ejecta and the passage of impact-generated shock waves.

If the crustal density was constant at all lunar radii beneath the deepest topographic excursion, our bulk density estimates would represent an average over the depths sampled by the topographic relief, which is on average about 4 km. Since the deeper crust would not generate lateral gravity variations in this model, this depth should be considered a minimum estimate for the depth scale of the GRAIL density determinations. If crustal porosity were solely a function of depth below the surface, the depth scale could be constrained using the relationship between gravity and topography in the spectral domain, since deep short-wavelength mass anomalies are attenuated faster than shallower and longer wavelength anomalies. Two models were investigated: one where the porosity decreased exponentially with depth below the surface, and another where a constant thickness porous layer overlies a non-porous basement (supplemental online materials). The $1-\sigma$ upper bound of both depth scales is largely unconstrained, with values greater than 30 km being able to fit the observations in most regions. $1-\sigma$ lower bounds for the two depth scales are constrained to be less than 31 km, which implies that at least some regions of the highlands have significant porosity extending 10s of kilometers deep into the crust, and perhaps into the uppermost mantle.

Our density and porosity estimates are broadly consistent with laboratory measurements of lunar feldspathic meteorites and feldspathic rocks collected during the Apollo missions. The average density of the most reliable of these measurements is $2580 \pm 170 \text{ kg m}^{-3}$ [14] (supplemental online materials), and the porosities of these samples vary from about 2 to 22% with an average of $8.6 \pm 5.3\%$. The ordinary chondrite meteorites have a similar range of porosities as the lunar samples, and this has been shown to be the result of impact-induced micro fractures [15]. A 1.5 km drill core in the Chicxulub impact crater shows that impact deposits have

porosities between 5 and 24%, whereas the basement rocks contain porosities up to 21% [16]. Gravity data over the Ries, Tvären and Granby terrestrial impact craters (with diameters of 23, 3 and 2 km) imply the existence of 10-15% excess porosity 1 km below the surface [17, 18], and for the Ries, about 7% porosity at 2-km depths. Whereas the impact induced porosities associated with these three craters are a result of single events, on the Moon, each region of the crust has been affected by numerous impacts.

Compression data of lunar igneous rocks show that the lithostatic pressures encountered in the crust and upper mantle are insufficient to close all fractures. About 2-3% porosity can be removed at the 4 kbar pressures encountered 100 km below the surface [19, 20], and the complete closure of pore space is instead likely to occur by viscous deformation at elevated temperatures. Given the exponential dependence of viscosity on temperature, and the increase in temperature with depth below the surface, porosity will be removed over a narrow depth interval [21]. Using representative temperature gradients over 4 billion years, this transition depth is predicted to lie between 50 and 110 km below the surface (supplemental online materials). Where the crust is thinner than these values, porosity could exist in the underlying mantle, as has been suggested by S-wave velocity profiles derived from the Apollo seismic data [22].

With our new constraints on crustal density and porosity, we construct a global crustal thickness model using GRAIL gravity and Lunar Reconnaissance Orbiter topography [23] data. Our model accounts for the gravitational signatures of the surface relief, relief along the crust-mantle interface, and the signal that arises from lateral variations in crustal grain density as predicted by remote sensing data (supplemental online materials). Crustal densities beneath the mare are extrapolated from the surrounding highland values, and by neglecting the thin veneer of dense basalts [11], the total crustal thicknesses could be biased locally by no more than a few km. As constraints to our model, we use end-member seismically determined thicknesses of 30 and 38 [22, 24] km near the Apollo 12 and 14 landing sites, and assume a minimum crustal

thickness near zero given that at least one impact event is likely to have excavated through the entire crust [11,25]. After choosing a porosity model of the crust, a unique model that fits the observations is obtained by varying the average crustal thickness and mantle density. Since some of the short wavelength gravity signal is a result of unmodeled crustal signals, our inversions make use of a spectral low-pass filter [26] near degree 80, yielding a spatial resolution that is 60% better than previous models [27]. Remote sensing data of impact crater central peaks imply some subsurface compositional variability, but do not require broad compositional layering [28], justifying our use of a model that is uniform in composition with depth.

For our first set of models, we assumed either that a constant thickness porous layer exists above bedrock or that the porosity decreases exponentially with depth. With a mantle grain density of 3360 kg m^{-3} [29], both models are incapable of fitting simultaneously the seismic and minimum thickness constraints as a result of the relatively small density contrast at the crust-mantle interface. For our second set of models, we assumed that the porosity of the entire crust was constant. With 12% porosity and the 30-km seismic constraint, an acceptable solution is found with an average crustal thickness of 34 km and a mantle density of 3220 kg m^{-3} (Fig. 3). For the 38-km constraint, values of 43 km and 3150 kg m^{-3} are found, respectively. By reducing the porosity to 7%, the mantle density increases by about 150 kg m^{-3} , but the average crustal thickness remains unchanged. Identical average crustal thicknesses are obtained using a crustal density map extrapolated from Fig. 1. The mantle densities should be considered representative to the greatest depths of the crust ($\sim 80 \text{ km}$ below the surface), and if the grain density of mantle materials is 3360 kg m^{-3} , then a maximum of 6% porosity could exist in the uppermost mantle.

Before GRAIL, the average thickness of the Moon's crust was thought to be close to 50 km [11,27] (supplemental online materials). Our revised estimates that are up to 16 km thinner have important implications for the abundance of refractory elements in the Moon, which is an important parameter for assessing processes that operated during lunar formation. Published

estimates [2] for the bulk silicate abundance of the refractory element aluminum fall into two categories: One group indicates that the Moon contains the same abundance as Earth, whereas the other suggests at least a 50% enrichment. Assuming that the lunar crust consists of an upper mixed layer 5-km thick containing 28 wt.% Al_2O_3 [2] with the remainder being nearly pure anorthosite (34 wt.% Al_2O_3), we calculate that a 34-km thick crust contributes 1.6 and 1.7 wt.% to the total bulk silicate abundance of Al_2O_3 for crustal porosities of 12 and 7%, respectively. A 43-km thick crust contributes 2.0 and 2.1 wt.%, respectively. The inclusion of more mafic materials in the lowermost crust has little effect on the average crustal abundance of aluminum [1]. In order for bulk lunar silicate aluminum abundances to match those for Earth (4 wt.% Al_2O_3), the lunar mantle would need to contain 1.9-2.4 wt.% Al_2O_3 , whereas a 50% enrichment in refractory elements would require mantle abundances of 4.1-4.5 wt.% Al_2O_3 . Petrologic assessments indicate mantle Al_2O_3 abundances close to 1-2 wt.% [30], supporting a lunar refractory element composition similar to Earth. Estimates derived from modeling the Apollo seismic data have a broad range, from 2.3-3.1 wt.% for the entire mantle [31], to 2.0 to 6.7 wt.% for the upper and lower mantle [32], respectively. Although further constraints on the composition of the deep lunar mantle are needed, the modest contribution to the bulk lunar Al_2O_3 from the crust does not require the Moon to be enriched in refractory elements.

Crustal thickness variations on the Moon are dominated by impact basins with diameters from 200 to 2000 km. With a thinner crust, it becomes increasingly probable that some of the largest impact events excavated through the entire crustal column and into the mantle [11]. Two impact basins have interior thicknesses near zero (Moscoviense and Crisium), and three others have thicknesses that are less than 5 km (Humboldtianum, Apollo, and Poincaré). Remote sensing data show atypical exposures of olivine-rich materials surrounding some lunar impact basins that could represent excavated mantle materials [25], and the most prominent of these are associated with the Crisium, Moscoviense, and Humboldtianum basins. Our crustal thickness

model strengthens the hypothesis that these impact events excavated into the mantle, and given the importance of the mantle in deciphering the origin and initial differentiation of the Moon, these exposures represent prime targets for future sample return missions.

Since the crust of the Moon has experienced only limited volcanic modification, and in addition lacks aqueous and atmospheric erosional processes, the Moon is an ideal recorder of processes that must have affected the crusts of all terrestrial planets at some point in their evolution. Large impact events were common in the first billion years of solar system history, and the crusts of the terrestrial planets would have been fractured to great depths, just as was the Moon. For Earth and Mars, this porosity could have hosted significant quantities of ground water over geologic time [33]. For planets lacking groundwater, such as Mercury, crustal porosity would significantly reduce the effective thermal conductivity, hindering the escape of heat to the surface, and affecting the planet's thermal and magmatic evolution [34].

Acknowledgements

The GRAIL mission is a component of the NASA Discovery Program and is performed under contract to the Massachusetts Institute of Technology and Jet Propulsion Laboratory. Additional support for this work was provided by the French Space Agency (CNES), the Centre National de la Recherche Scientifique, and the UnivEarthS project of Sorbonne Paris Cité.

References

- [1] S. Yamamoto, *et al.*, *Geophys. Res. Lett.* **39**, L13201 (2012).
- [2] S. R. Taylor, G. J. Taylor, L. A. Taylor, *Geochim. Cosmo. Acta* **70**, 5904 (2006).
- [3] R. M. Canup, *Icarus* **196**, 518 (2008).
- [4] W. F. Bottke, *et al.*, *Nature* **485**, 78 (2012).

- [5] C. I. Fassett, *et al.*, *J. Geophys. Res.* **117**, 0 (2012).
- [6] A. S. Konopliv, S. W. Asmar, D. N. Yuan, *Icarus* **150**, 1 (2001).
- [7] K. Matsumoto, *et al.*, *J. Geophys. Res.* **115**, E06007 (2010).
- [8] M. T. Zuber, *et al.*, *Space Sci. Rev.* **submitted** (2012).
- [9] M. T. Z. et al., *Science* **this issue** (2012).
- [10] P. Lucey, *et al.*, *New views of the Moon*, B. J. Jolliff, M. A. Wieczorek, C. K. Shearer, C. R. Neal, eds. (Mineral. Soc. Amer., 2006), vol. 60 of *Rev. Min. Geochem.*, pp. 83–219.
- [11] M. A. Wieczorek, *et al.*, *New views of the Moon*, B. J. Jolliff, M. A. Wieczorek, C. K. Shearer, C. R. Neal, eds. (Mineral. Soc. Amer., 2006), vol. 60 of *Rev. Min. Geochem.*, pp. 221–364.
- [12] Q. Huang, M. A. Wieczorek, *J. Geophys. Res.* **117**, E05003 (2012).
- [13] T. H. Prettyman, *et al.*, *J. Geophys. Res.* **111**, E12007 (2006).
- [14] W. Kiefer, R. J. Macke, D. T. Britt, A. J. Irving, G. J. Consolmagno, *Geophys. Res. Lett.* **39**, L07201 (2012).
- [15] G. Consolmagno, D. Britt, R. Macke, *Chemie der Erde / Geochemistry* **68**, 1 (2008).
- [16] T. Elbra, L. J. Pesonen, *Meteoritics and Planetary Science* **46**, 1640 (2011).
- [17] J. Pohl, D. Stoeffler, H. Gall, K. Ernstson, *Impact and Explosion Cratering: Planetary and Terrestrial Implications*, D. J. Roddy, R. O. Pepin, R. B. Merrill, eds. (1977), pp. 343–404.
- [18] H. Henkel, T. C. Ekenligoda, S. Aaro, *Tectonophysics* **485**, 290 (2010).

- [19] D. R. Stephens, E. M. Lilley, *Geochim. Cosmochim. Acta Suppl., Proc. Apollo 11 Lunar Sci. Conf.* **1**, 2427 (1970).
- [20] D. R. Stephens, E. M. Lilley, *Proc. Lunar Planet. Sci. Conf.* **2**, 2165 (1971).
- [21] F. Nimmo, R. T. Pappalardo, B. Giese, *Icarus* **166**, 21 (2003).
- [22] P. Lognonné, J. Gagnepain-Beyneix, H. Chenet, *Earth Planet. Sci. Lett.* **211**, 27 (2003).
- [23] D. E. Smith, *et al.*, *Geophys. Res. Lett.* **37**, L18204 (2010).
- [24] A. Khan, K. Mosegaard, *J. Geophys. Res.* **107**, 10.1029/2001JE001658 (2002).
- [25] S. Yamamoto, *et al.*, *Nature Geosci.* **3**, 533 (2010).
- [26] M. A. Wieczorek, R. J. Phillips, *J. Geophys. Res.* **103**, 1715 (1998).
- [27] Y. Ishihara, *et al.*, *Geophys. Res. Lett.* **36**, L19202 (2009).
- [28] J. T. S. Cahill, P. G. Lucey, M. A. Wieczorek, *J. Geophys. Res.* **114**, E09001 (2009).
- [29] R. Garcia, J. Gagnepain-Beyneix, S. Chevrot, P. Lognonné, *Phys. Earth Planet. Int.* **188**, 96 (2011).
- [30] S. Mueller, G. J. Taylor, R. J. Phillips, *J. Geophys. Res.* **93**, 6338 (1988).
- [31] A. Khan, J. A. D. Connolly, J. MacLennan, K. Mosegaard, *Geophys. J. Int.* **168**, 243 (2007).
- [32] O. L. Kuskov, V. A. Kronrod, *Phys. Earth Planet. Inter.* **107**, 285 (1998).
- [33] S. M. Clifford, *J. Geophys. Res.* **98**, 10973 (1993).
- [34] S. Schumacher, D. Breuer, *J. Geophys. Res.* **111**, E02006 (2006).

- [35] M. A. Wieczorek, *Treatise on Geophysics*, T. Spohn, G. Schubert, eds. (Elsevier-Pergamon, Oxford, 2007), vol. 10, pp. 165–206.
- [36] D. L. Turcotte, R. J. Willemann, W. F. Haxby, J. Norberry, *J. Geophys. Res.* **86**, 3951 (1981).
- [37] D. E. Wilhelms, *The geologic history of the Moon*, vol. 1348 (U.S. Geol. Surv. Spec. Pap., 1987).
- [38] H. J. Melosh, *Impact Cratering: A Geologic Process* (Oxford Univ. Press, New York, 1989).
- [39] M. A. Wieczorek, F. J. Simons, *Geophys. J. Int.* **162**, 655 (2005).
- [40] F. J. Simons, F. A. Dahlen, M. A. Wieczorek, *SIAM Rev.* **48**, 504 (2006).
- [41] M. A. Wieczorek, F. J. Simons, *J. Fourier Anal. Appl.* **13**, 665 (2007).
- [42] W. S. Kiefer, R. J. Macke, D. T. Britt, A. J. Irving, G. J. Consolmagno, *Second Conf. Lunar Highlands Crust* p. abstract 9006 (2012).
- [43] R. Korotev, *Chemie der Erde, Geochemistry* **65**, 297 (2005).
- [44] M. Ohtake, *et al.*, *Nature Geosci.* **5**, 384 (2012).
- [45] R. J. Macke, D. T. Britt, G. J. Consolmagno, *Planet. Space Sci.* **58**, 421 (2010).
- [46] J. Eluszkiewicz, *Icarus* **170**, 234 (2004).
- [47] E. Rybacki, G. Dresen, *J. Geophys. Res.* **105**, 26017 (2000).
- [48] S. Karato, P. Wu, *Science* **260**, 771 (1993).
- [49] J. R. Driscoll, D. M. Healy, *Adv. Appl. Math.* **15**, 202 (1994).

- [50] M. N. Toksöz, A. M. Dainty, S. C. Solomon, K. R. Anderson, *Rev. Geophys.* **12**, 539 (1974).
- [51] M. T. Zuber, D. E. Smith, F. G. Lemoine, G. A. Neumann, *Science* **266**, 1839 (1994).
- [52] G. A. Neumann, M. T. Zuber, D. E. Smith, F. G. Lemoine, *J. Geophys. Res.* **101**, 16,841 (1996).
- [53] A. Khan, K. Mosegaard, K. K. L. Rasmussen, *Geophys. Res. Lett.* **27**, 1591 (2000).
- [54] H. Chenet, P. Lognonné, M. Wieczorek, H. Mizutani, *Earth Planet. Sci. Lett.* **243**, 1 (2006).
- [55] H. Hikida, M. A. Wieczorek, *Icarus* **192**, 150 (2007).

Supporting Online Material

www.sciencemag.org

SOM Text

Table S1

Figs. S1 to S12

References (35-55)

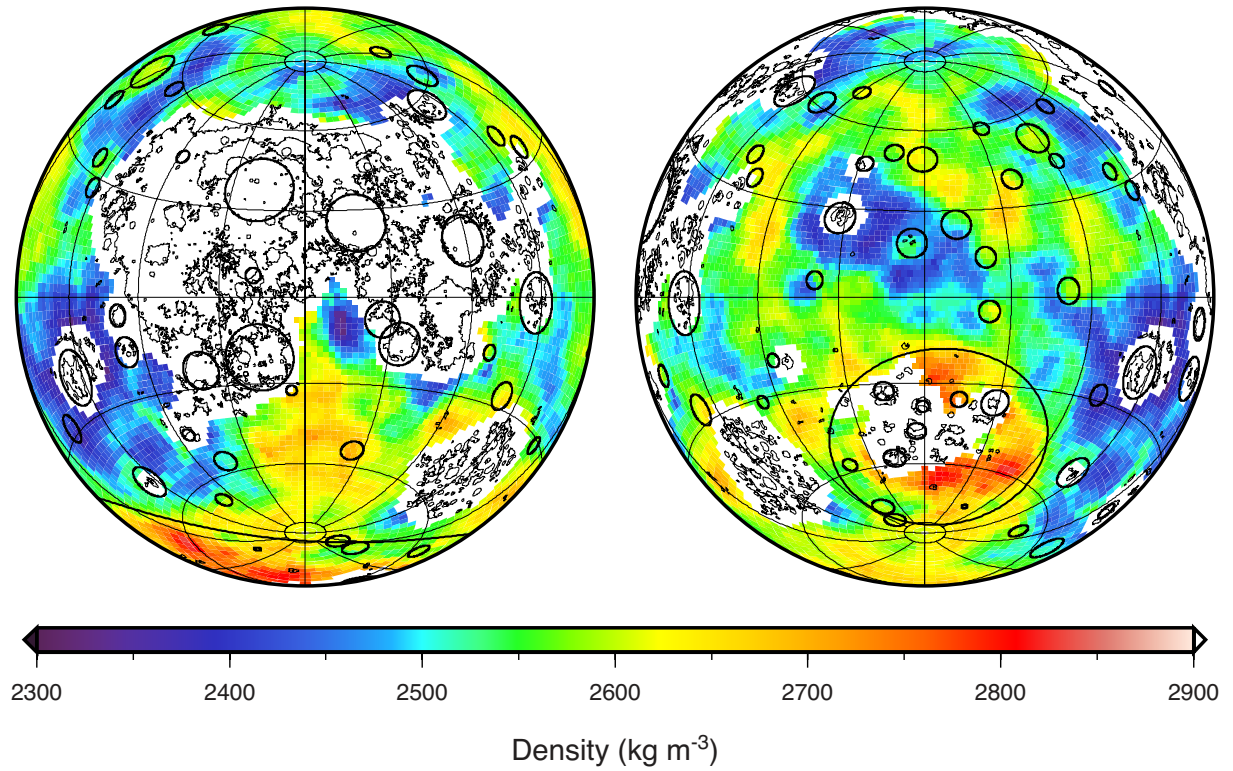


Fig. 1. Bulk density of the lunar crust from gravity and topography data. At each point on a 60-km equally spaced grid, the bulk density was calculated within 360 km diameter circles (spanning 12° of latitude). Thin lines outline the mare basalts, and solid circles correspond to prominent impact basins, whose diameters are taken as the region of crustal thinning in Fig. 3. The largest farside basin is the South Pole-Aitken basin. Data are presented in two Lambert azimuthal equal-area projections centered over the near (left) and far (right) side hemispheres, with each image covering 75% of the lunar surface, and with gridlines being spaced every 30° . Names of prominent impact basins are annotated in Fig. 3.

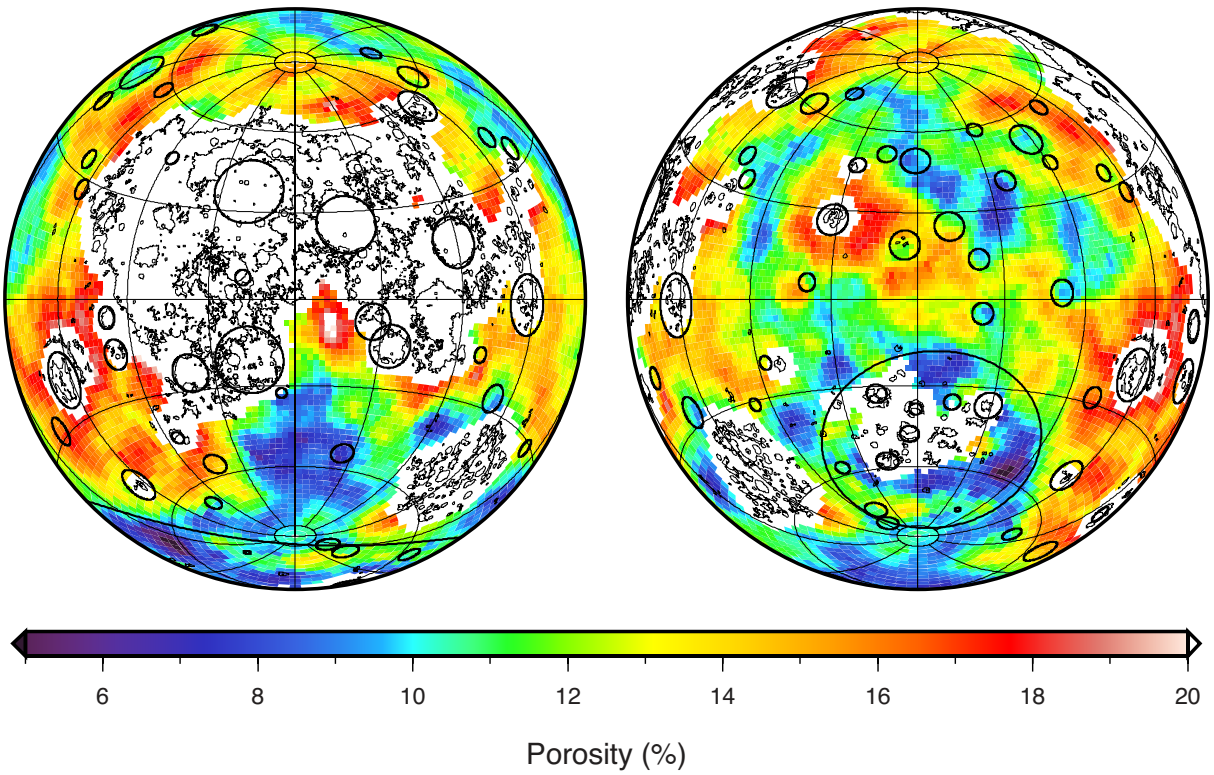


Fig. 2. Porosity of the lunar crust, with bulk density from GRAIL and grain density from sample and remote-sensing analyses. Image format the same as in Fig. 1.

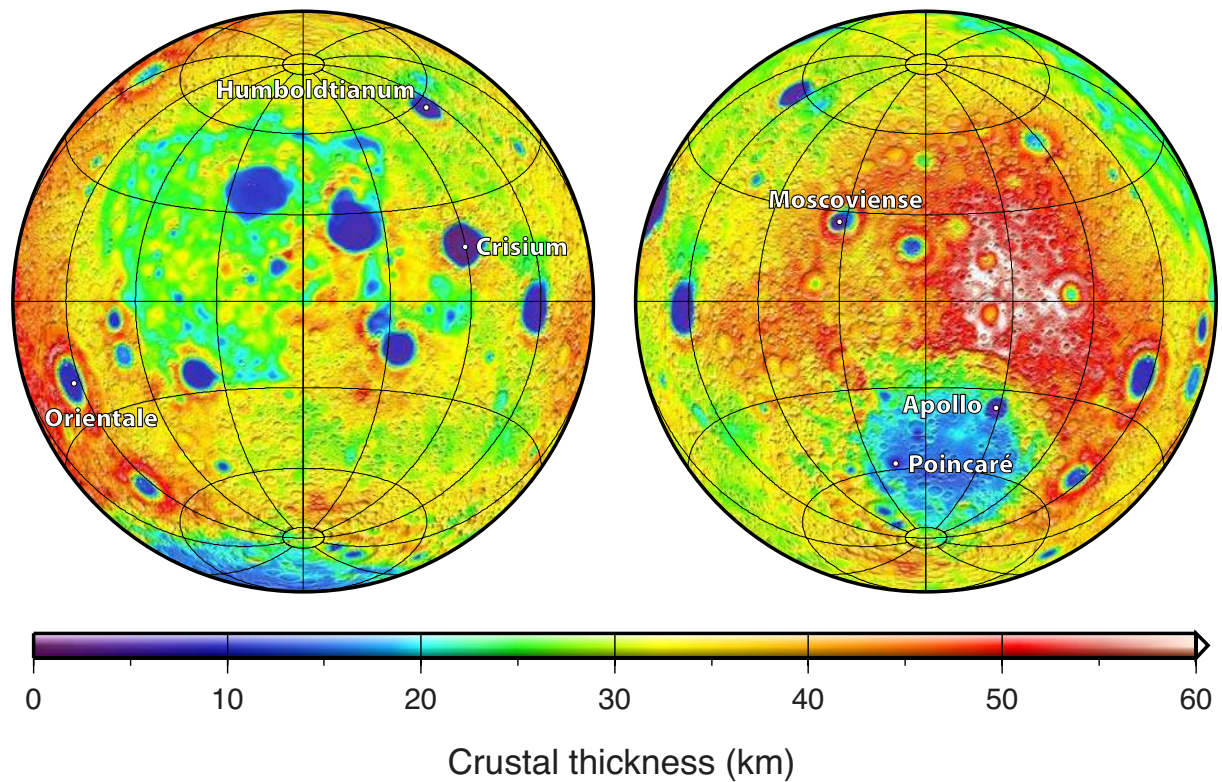


Fig. 3. Crustal thickness of the Moon from GRAIL gravity and Lunar Reconnaissance Orbiter topography. With a crustal porosity of 12% and a mantle density of 3220 kg m^{-3} , the minimum crustal thickness is less than 1 km in the interior of the farside basin Moscoviense, and the thickness at the Apollo 12 and 14 landing sites is 30 km. Image format the same as in Fig. 1, and each image is overlain by a shaded relief map derived from the surface topography.

1 Density and porosity of the lunar crust from gravity and topography

The gravitational potential exterior to a planet can be expressed as [35]

$$U(\mathbf{r}) = \frac{GM}{r} \sum_{l=0}^{\infty} \sum_{m=-l}^l \left(\frac{R_0}{r}\right)^l C_{lm} Y_{lm}(\theta, \phi), \quad (1)$$

where \mathbf{r} is position, G is the gravitational constant, M is the mass of the planet, R_0 is the reference radius of the spherical harmonic coefficients C_{lm} of degree l and order m , Y_{lm} are the 4π -normalized spherical harmonic functions, and θ and ϕ are colatitude and longitude, respectively. In this harmonic form, eq. (1) is exact for all radii greater than the maximum topographic excursion of the planet. If the relief h with respect to a spherical interface of radius D is expressed in spherical harmonics as

$$h(\theta, \phi) = \sum_{l=0}^{\infty} \sum_{m=-l}^l h_{lm} Y_{lm}(\theta, \phi), \quad (2)$$

the spherical harmonic coefficients of the gravitational potential resulting from a density contrast $\rho(\theta, \phi)$ can be calculated to arbitrary precision by the expression [26,35]

$$C_{lm} = \frac{4\pi D^3}{M(2l+1)} \sum_{n=1}^N \frac{(\rho h^n)_{lm}}{D^n n!} \frac{\prod_{j=1}^n (l+4-j)}{(l+3)}, \quad (3)$$

where the spherical harmonic coefficients of ρh^n are calculated according to

$$(\rho h^n)_{lm} = \frac{1}{4\pi} \int_{\Omega} [\rho(\theta, \phi) h^n(\theta, \phi)] Y_{lm}(\theta, \phi) d\Omega. \quad (4)$$

We use $N = 7$ when evaluating eq. (3), which gives a relative precision better than 10^{-4} at degree 400 for the surface relief of the Moon. The radial component of the gravity field is obtained by taking the radial derivative of eq. (1), and using the sign convention that gravity is positive when directed downwards, this is

$$g(\mathbf{r}) = \frac{GM}{r^2} \sum_{l=0}^{\infty} \sum_{m=-l}^l \left(\frac{R_0}{r}\right)^l (l+1) C_{lm} Y_{lm}(\theta, \phi). \quad (5)$$

The height of an equipotential surface above a reference radius R is, to first order,

$$N(\theta, \phi) \approx R \sum_{l=1}^{\infty} \sum_{m=-l}^l \left(\frac{R_0}{R} \right)^l C_{lm} Y_{lm}(\theta, \phi). \quad (6)$$

The degree-dependent relation between gravity g and topography h is quantified by the admittance

$$Z(l) = \frac{S_{hg}(l)}{S_{hh}(l)}, \quad (7)$$

and spectral correlation

$$\gamma(l) = \frac{S_{hg}(l)}{\sqrt{S_{hh}(l)S_{gg}(l)}}, \quad (8)$$

where the (cross)-power spectra S are

$$S_{hg}(l) = \sum_{m=-l}^l h_{lm} g_{lm}, \quad (9)$$

$$S_{hh}(l) = \sum_{m=-l}^l h_{lm} h_{lm}, \quad (10)$$

$$S_{gg}(l) = \sum_{m=-l}^l g_{lm} g_{lm}. \quad (11)$$

The observed gravity field of the Moon is a result of many factors, including surface topography, relief along the crust-mantle interface, core flattening, and heterogeneities in both the crust and mantle. Loads on the lithosphere, such as surface topography and volcanic intrusions, will cause the lithosphere to flex, giving rising to a signal from the crustal-mantle interface. Since gravitational signals are attenuated with increasing height above their depth of origin, and since the amount of flexure decreases with decreasing wavelength, the shortest wavelength anomalies will be sensitive primarily to relief along the surface. We quantify the influence of lithospheric flexure on the observed gravity field using a lithospheric loading model that incorporates surface loads on a thin elastic shell [36]. For this model, the admittance Z is simply the ratio of the gravity and topography coefficients in the spectral domain, and the spectral correlation γ is unity at all degrees.

For demonstration purposes, we use only the first order term in eq. (3), and calculate the admittance for several values of the elastic thickness T_e . As shown in Fig. S1, the admittance depends strongly on the elastic thickness at low degrees, but at high degrees, the admittance approaches an asymptotic value that is proportional to the crustal density. For elastic thicknesses greater than 5 km, the contribution to the gravity signal from lithospheric flexure is seen to be negligible at degrees greater than about 100. Even for an elastic thickness of zero, the admittance differs by less than 1% from that of a rigid shell at degrees greater than 170. Since it is unlikely that the elastic thickness would be zero for the shortest wavelengths, which are dominated by young impact craters, we neglect the flexural signal by analyzing degrees greater than 150.

Even though the GRAIL gravity field has been developed up to degree and order 420, the highest degree terms are biased by noise and incomplete sampling between adjacent orbital tracks. In Fig. S2, we plot the power spectrum of the gravity field, the measurement noise, the gravitational contribution from the surface topography (the Bouguer correction), and the gravitational signal that remains after removing the topographic contribution (the Bouguer anomaly). Beyond degree 320, the power spectrum of the Bouguer anomaly increases in amplitude and follows the gravitational error. In order to minimize the consequences of noise from the gravity field in our analysis, we make use of degrees less than 310.

If the density of the crust ρ_c were constant, the observed gravity g at short wavelengths would be equal to the sum of the Bouguer correction g^{BC} and the measurement noise g^{noise} . If the correct crustal density were chosen when calculating the Bouguer correction, the Bouguer anomaly g^{BA} would simply be equal to the noise in the gravity model

$$g_{lm}^{\text{BA}}(\rho_c) = g_{lm} - g_{lm}^{\text{BC}}(\rho_c) = g_{lm}^{\text{noise}}. \quad (12)$$

Since the gravitational measurement noise should be uncorrelated with the surface topography,

an unbiased estimate of the crustal density is obtained by finding the value that minimizes the correlation between the Bouguer anomaly and topography.

We calculate the correlation coefficient of the gravity and topography in the space domain using gridded Bouguer gravity and topography within a spherical cap of a specified diameter. The gravity and topography coefficients are truncated below degree 150 and above degree 310, the gravity is downward continued to the average radius of the analysis region, and the gridded data are weighted by their associated areas. To neglect the gravitational contribution from the mare basalts, which are more dense than the highlands and which pool at low elevations, we neglect data points that lie with the mare using the map of ref. [37]. To assure that each analysis is based on similar effective areas, we neglect those analyses where more than 5% of the data have been discarded. Analyses were centered on a 60-km (2° of latitude) equally spaced grid, and the crustal density was varied to find the value that minimizes the absolute value of the correlation coefficient.

Estimates of the uncertainties in our density determinations were obtained by Monte Carlo modeling. Using of the known uncertainties of the global gravity field coefficients, noise in the Bouguer gravity field was simulated, and the probability distribution for the correlation coefficient between this noise and the topography was obtained. $1-\sigma$ error limits on the density were determined using the 68% confidence limits from the correlation coefficient probability distribution. To neglect regions with large uncertainties, a small number of analyses were discarded where the minimum correlation coefficient was greater than the 95% confidence limit.

Having calculated the bulk density from gravity and topography, we estimate the crustal porosity using independent estimates of the crustal grain density. An empirical correlation between grain density (estimated from a mineralogical norm) and the abundance of FeO and TiO₂ was obtained by ref. [12] for a large range of lunar rock compositions, including the ferroan anorthosites, Mg suite, alkali suite, KREEP basalts, impact melts, granulitic breccias,

mare basalts and volcanic glasses. The mineralogical grain density estimates have been shown to be accurate to 20 kg m^{-3} by direct measurements using helium pycnometry techniques [14], and the correlation with iron and titanium abundances has an intrinsic uncertainty of 45 kg m^{-3} for the entire suite of lunar rocks. Using Lunar Prospector gamma-ray spectrometer derived iron and titanium abundances [13], which are representative of the upper meter of the surface, our global crustal grain density estimate is shown in Fig. S3. For each region in our gravity analyses, the average grain density was calculated, from which the porosity ϕ was determined from the relation

$$\phi = 1 - \rho_{\text{bulk}} / \rho_{\text{grain}}, \quad (13)$$

where the bulk density is the density obtained from the gravity analysis. Since impact craters excavate materials to depths that are about one-tenth of the crater diameter [38], the composition of the lunar surface is likely to be representative of the underlying crust for most regions of the Moon. Nevertheless, where the crustal composition changes laterally, such as between the highlands and South Pole-Aitken basin, or between the highlands and mare basalts, ejecta from one compositional unit may overlie surface materials of a different composition.

Histograms of our results using 360-km diameter analysis regions are shown in Fig. S4 for the bulk density, bulk density uncertainty, and porosity. Our bulk density and porosity determinations are insensitive to variations in the filter applied to the gravity and topography by more than ± 50 degrees, as well as to changes in the size of the analysis region by a factor of two. Nevertheless, as the analysis region decreases in size, the uncertainties in the individual density determinations increase in magnitude. Porosity maps derived using several different sizes for the analysis regions are shown in Fig. S5.

We verify the accuracy of our bulk density determinations using an alternative analysis method that makes use of the relation between gravity and topography in the spectral domain. Since the gravity contribution from topography at high degrees is a non-linear function of the

topography, we model the observed gravity in terms of the gravity contribution from surface relief of unit density, \hat{g} ,

$$g_{lm}^{obs} = \rho_c \hat{g}_{lm} + I_{lm}, \quad (14)$$

where I_{lm} is that portion of the signal not predicted by the model, and which is assumed to be uncorrelated with \hat{g} . Multiplying both sides by \hat{g}_{lm} , summing over all degrees, and taking the expectation with respect to I , we obtain an unbiased estimate for the crustal density at each degree,

$$\rho_c(l) = \frac{S_{g^{obs}\hat{g}}(l)}{S_{\hat{g}\hat{g}}(l)}. \quad (15)$$

This equation is analogous to the admittance between gravity and topography from eq. (7).

We spatially localize the free-air gravity and gravity from unit density topography using the spherical Slepian functions of refs [39–41] and then compute the localized degree-dependent admittance and correlation functions, eqs (14) and (8). The spectral bandwidth L of the window was chosen to ensure that more than 99% of its power was localized within a spherical cap of a specified diameter. Since each degree l of the localized power spectrum has contributions from the global field from degrees $l - L$ to $l + L$, we calculate the average density for all degrees between $150 + L$ and $310 - L$. As the localized correlation should be nearly unity for uncompensated topography, those degrees with localized correlations less than 0.98 were discarded. If more than half of the degrees available for analysis were discarded, or if the analysis region contained more than 5% mare basalts, the analysis was discarded as well.

Our bulk density estimates using this spectral approach are shown in Fig. S6 using a localization window with a diameter of 540 km and a spectral bandwidth of $L = 28$. The average density of the highlands is found to be identical to that obtained from our space domain analysis. Minor differences in the lateral variations exist between Figs 1 and S6 that are a result of slightly different aspects of the two analysis techniques: The spectral approach is not capable of removing small regions of mare basalts in an analysis region, the spatio-spectral localization

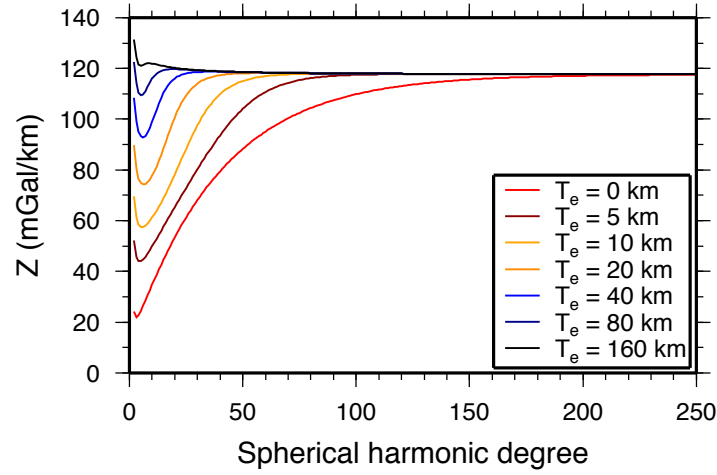


Fig. S1. Gravitational admittance as a function of spherical harmonic degree for a lithospheric loading model that includes surface loads on a thin elastic spherical shell. The admittance is sensitive to the assumed elastic thickness at low degrees, but approaches an asymptotic value that is proportional to the crustal density at high degrees.

window is not uniform in amplitude like the ‘box car’ window used in the space domain analysis, and since the gravity signal is largest at the lowest degrees, the space domain analysis is somewhat more sensitive to the lowest degrees (Fig. S2), whereas the spectral approach weights each degree evenly.

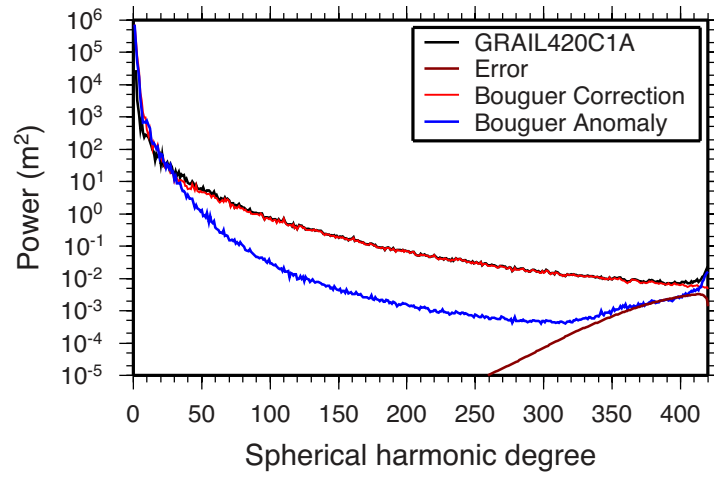


Fig. S2. Geoid power spectra of the GRAIL gravity model, the model errors, the Bouguer correction, and the Bouguer anomaly. Beyond degree 320, the Bouguer anomaly increases in amplitude and follows the model error spectrum.

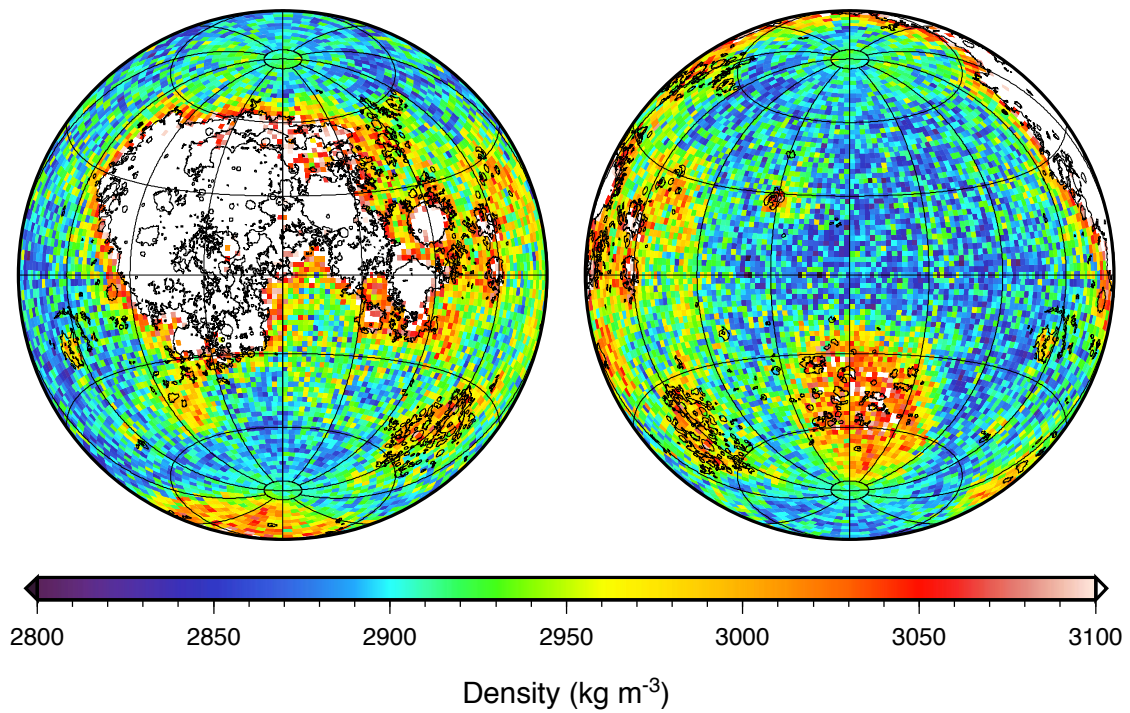


Fig. S3. Crustal grain density estimated from the 2° Lunar Prospector iron and titanium abundances and a sample-based empirical correlation between grain density and composition. Thin lines outline the locations of the mare basalts. Data are presented in two Lambert azimuthal equal-area projections centered over the near (left) and far (right) side hemispheres, with each image covering 75% of the lunar surface, and with gridlines being spaced every 30°.

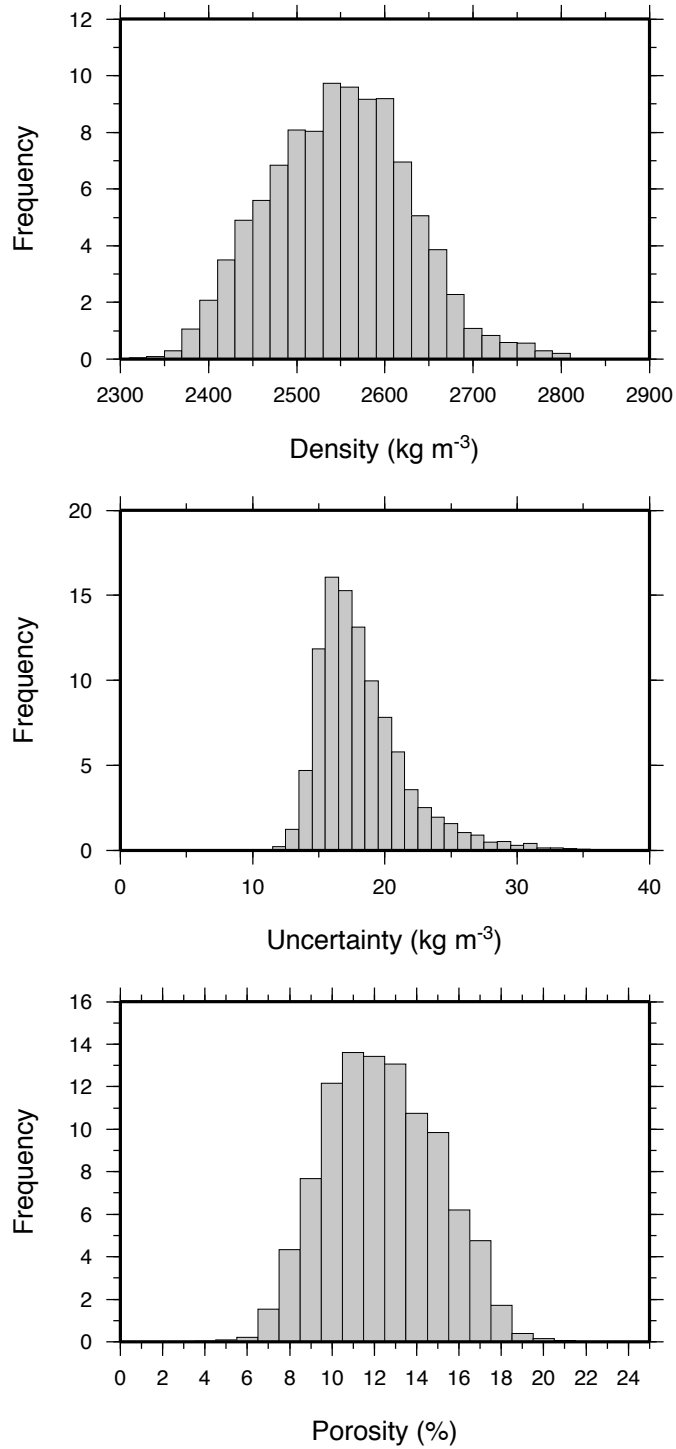


Fig. S4. Histograms of bulk density, bulk density uncertainty, and porosity for the lunar highlands using Bouguer gravity and topography within 360-km diameter circles.

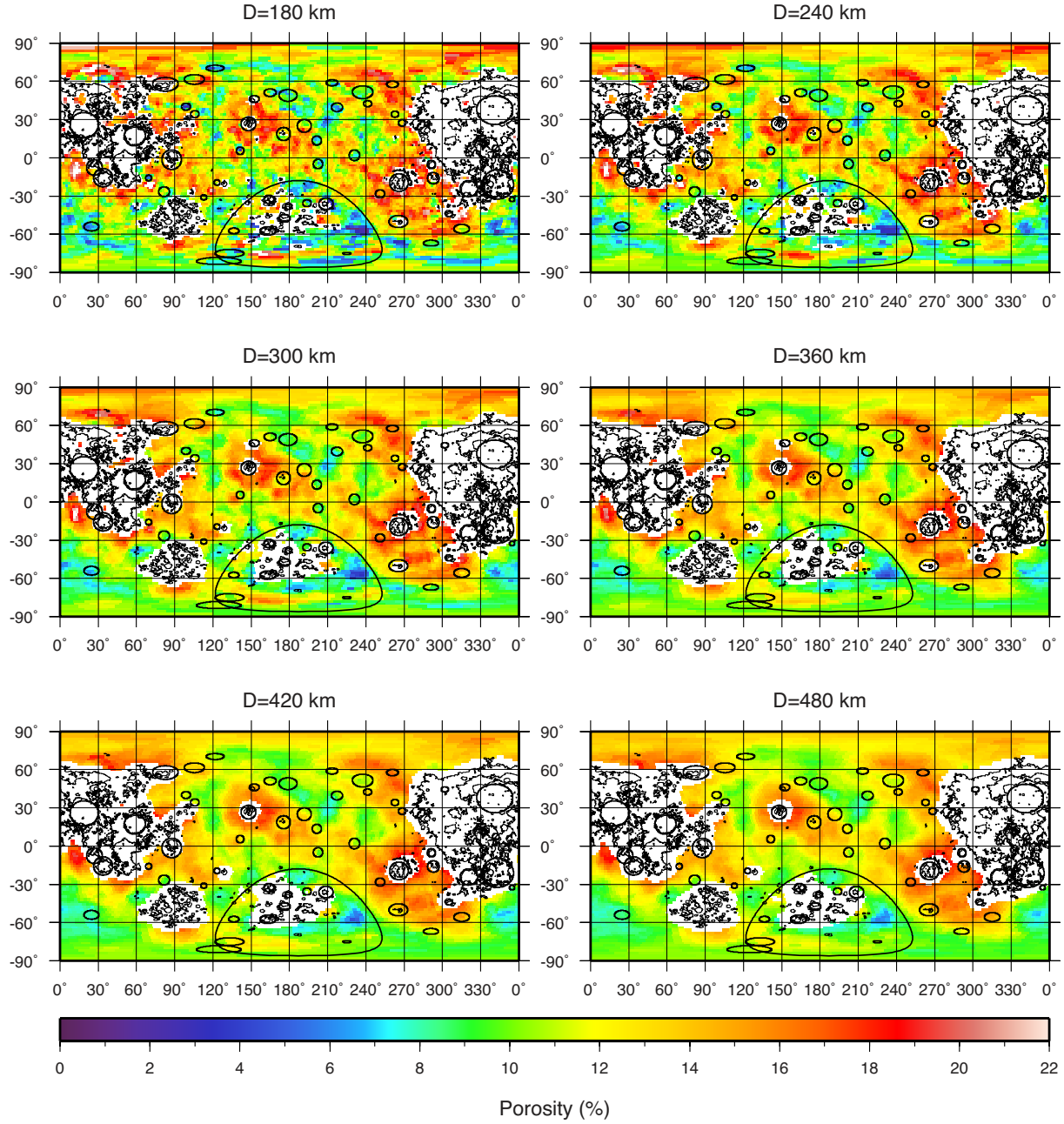


Fig. S5. Porosity of the lunar crust from gravity, topography, and independent grain density estimates. Thin lines outline the mare basalts, and circles denote the region of crustal thinning for prominent impact basins from Fig. 3. Bulk densities and porosities were calculated using data within circles with diameters of 180, 240, 300, 360, 420, 480 km, which corresponds to 6, 8, 10, 12, 14, and 16 degrees of latitude, respectively. All images are shown in a cylindrical projection centered over the far side hemisphere.

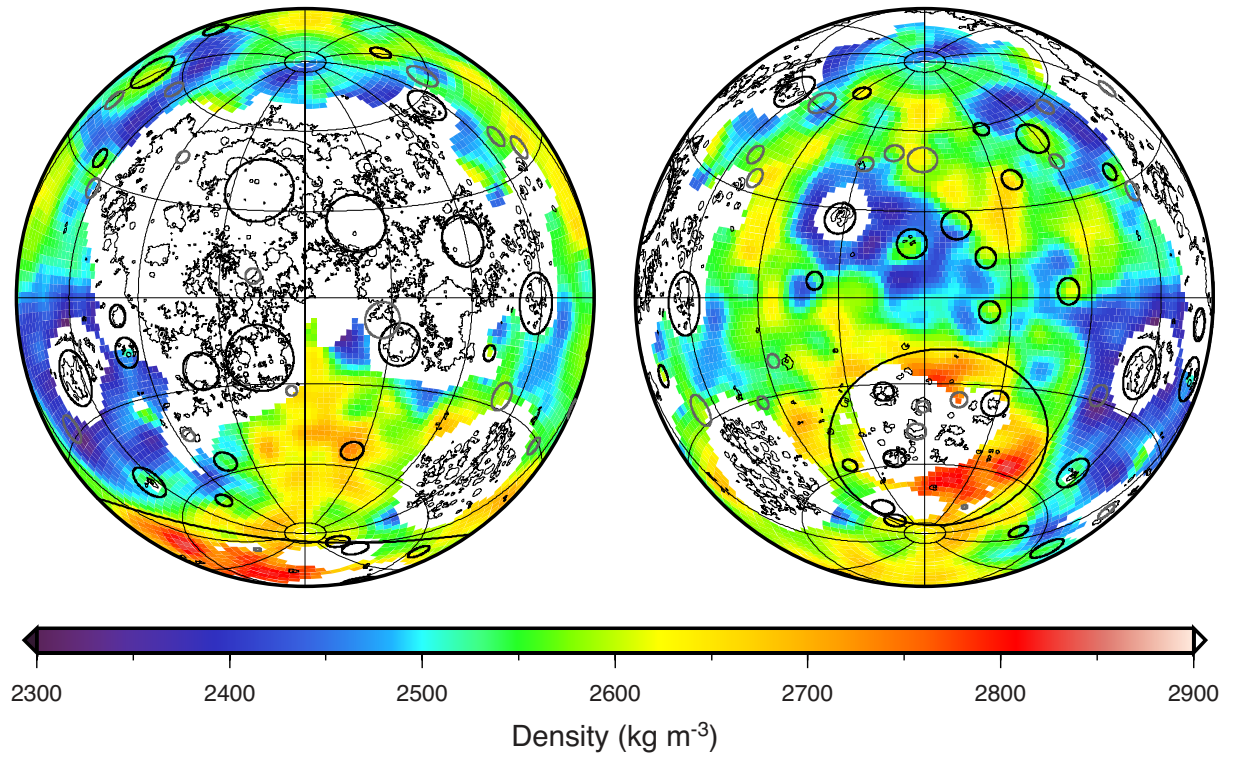


Fig. S6. Bulk density of the lunar crust from a localized spectral analysis approach. At each point on a 60-km equally spaced grid, the free-air gravity and predicted gravity from topography with unit density were multiplied by a localization window with a diameter of 540 km (18° of latitude). The bulk density was determined as the average of eq. (15). Image format the same as Fig. S3.

2 Depth dependence of porosity

If the density of the lunar crust were constant with depth, eq. (3) could be used to calculate the gravity above the surface. This is was the basis of our bulk crustal density determinations described in Section 1. If the crustal density were instead a function of depth below the surface, the lateral variations in density along a spherical interface below the surface would give rise to an additional gravitational signal. These gravity signals would be attenuated both with increasing depth and with increasing spherical harmonic degree (see eq. (1)). We use the wavelength dependence of this subsurface signal to investigate the subsurface density profile. Two models were investigated: one where the porosity decreased exponentially with depth below the surface, and another where a constant thickness porous layer overlies a non-porous basement. By discretizing the density profile in depth, the expected gravitational signature can be calculated to arbitrary precision from eq. (3) for each layer. We calculate the synthetic admittance for each density profile, and then compare this to observations.

Synthetic admittance functions are shown in Fig. S7 for several assumed porosity structures of the crust, all which assume a grain density of 2900 kg m^{-3} . Two end-member models with zero and 12% porosity are seen to be related by a simple multiplicative constant involving the ratio of the two bulk densities. The other models have density profiles and admittances bracketed by these end members. For one set of models, we assume that a 5 or 30 km thick layer with 12% porosity overlies non-porous bedrock. At small degrees, the admittance approaches the value predicted for the zero porosity model, whereas at the largest degrees, the admittance approaches the value predicted for the constant 12% porosity model. This is easily understood as the shortest wavelength signals become increasingly attenuated with increasing depth below the surface. At the shortest wavelengths, the gravity field is simply a result of the density of the surface relief. Models that utilize an exponential decrease in porosity with depth yield very

similar results if the depth of the porous layer D is replaced by the e -folding depth λ , and if the porosity of the layer ϕ is replaced by the porosity at the surface ϕ_0 .

For illustrative purposes, we calculate the global effective density from eq. (15) for a layer of thickness D and porosity ϕ under the assumption that the grain density is 2915 kg m^{-3} . This function gives the effective bulk density at each degree that would be obtained if it were assumed that the density of the crust was uniform. The rms misfit between this effective density and that obtained using the observed gravity field is shown in Fig. S8 using degrees between 150 and 310. A clear tradeoff is found between these two parameters, but a best fit is found for a layer thickness of 28 km and a porosity of 13%. Given that the gravity signal for the shortest wavelengths is attenuated with increasing depth, the admittance is largely insensitive to layer thickness in excess of about 30 km. Similar results are found for a model where the porosity decreases exponentially with depth.

We next use a spatio-spectral localization technique to calculate localized admittances, and then use Monte Carlo methods to estimate the $1\text{-}\sigma$ upper and lower bounds for the layer thickness and porosity. The procedure used is similar to that described in Section 1, except that here we use a localization window with a diameter of 900 km (corresponding to 30° of latitude). By employing a larger window size, the spectral bandwidth of the window is reduced to $L = 17$, and this gives us a higher spectral resolution and a greater number of localized admittances to analyze. In Fig. S9, we plot the best-fit layer thickness and porosity, as well as the $1\text{-}\sigma$ upper and lower bounds. The porosity is found to be rather well constrained and is consistent with our analyses in Section 1. In contrast, the layer depth is not well constrained. For most of the highlands, the $1\text{-}\sigma$ upper bound is simply greater than about 40 km. Nevertheless, the $1\text{-}\sigma$ lower bound possess values from about zero to 31 km, implying that some regions of the Moon possess a porous layer that is 10s of km thick.

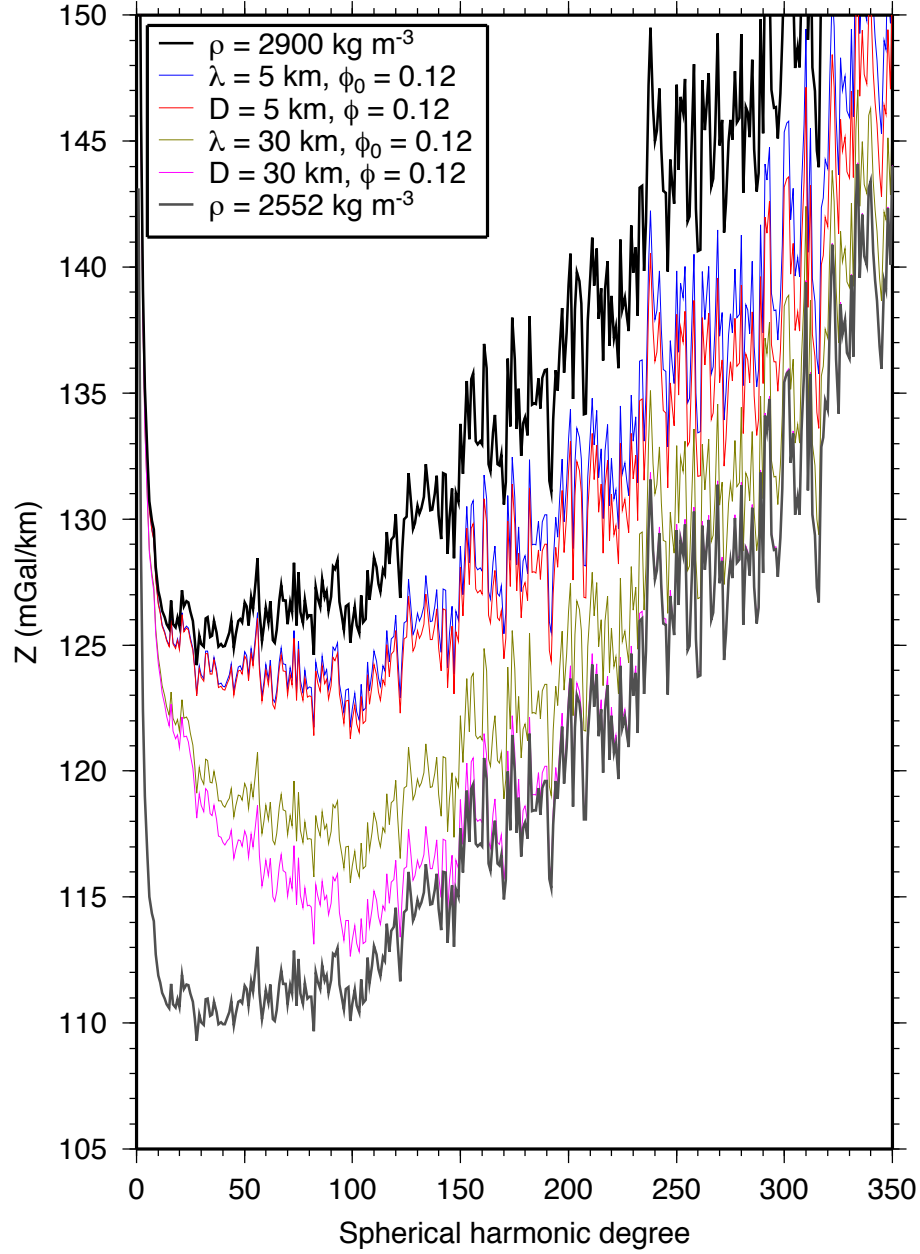


Fig. S7. Synthetic admittances predicted by several assumed density profiles of the highlands crust. Black and gray curves represent end-member cases with a constant bulk density of 2900 and 2552 kg m⁻³, respectively. Red and magenta curves are for models where a layer of thickness D and porosity ϕ overlie non-porous bedrock. Blue and green curves are for models where the porosity decreases exponentially with depth with e -folding depth λ and surface porosity ϕ_0 .

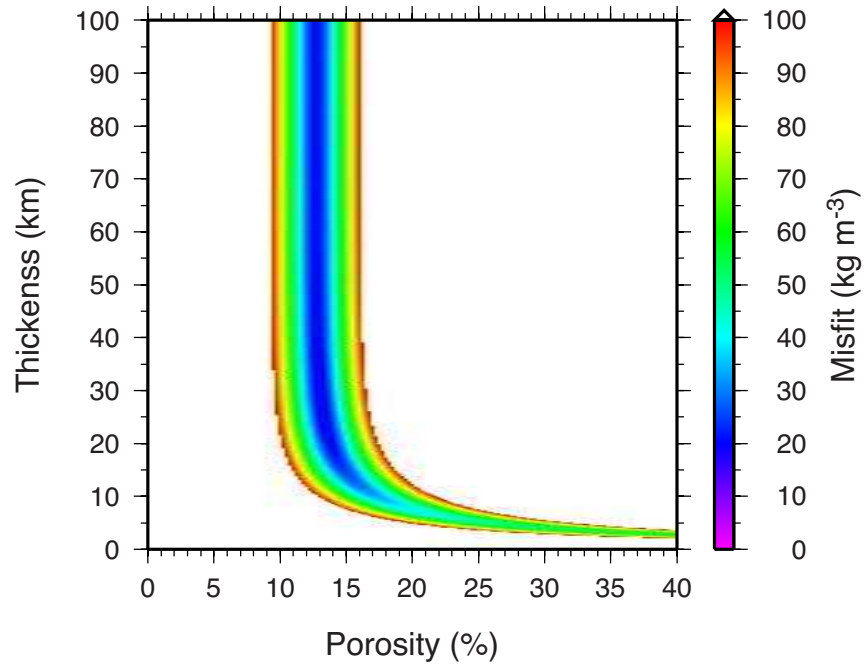


Fig. S8. RMS misfit for a model with a layer of constant thickness and porosity overlying non-porous bedrock. The misfit is the rms difference of the effective density $\rho_c(l)$ calculated from eq. (15) using both the model and observed gravity between degrees 150 and 310.

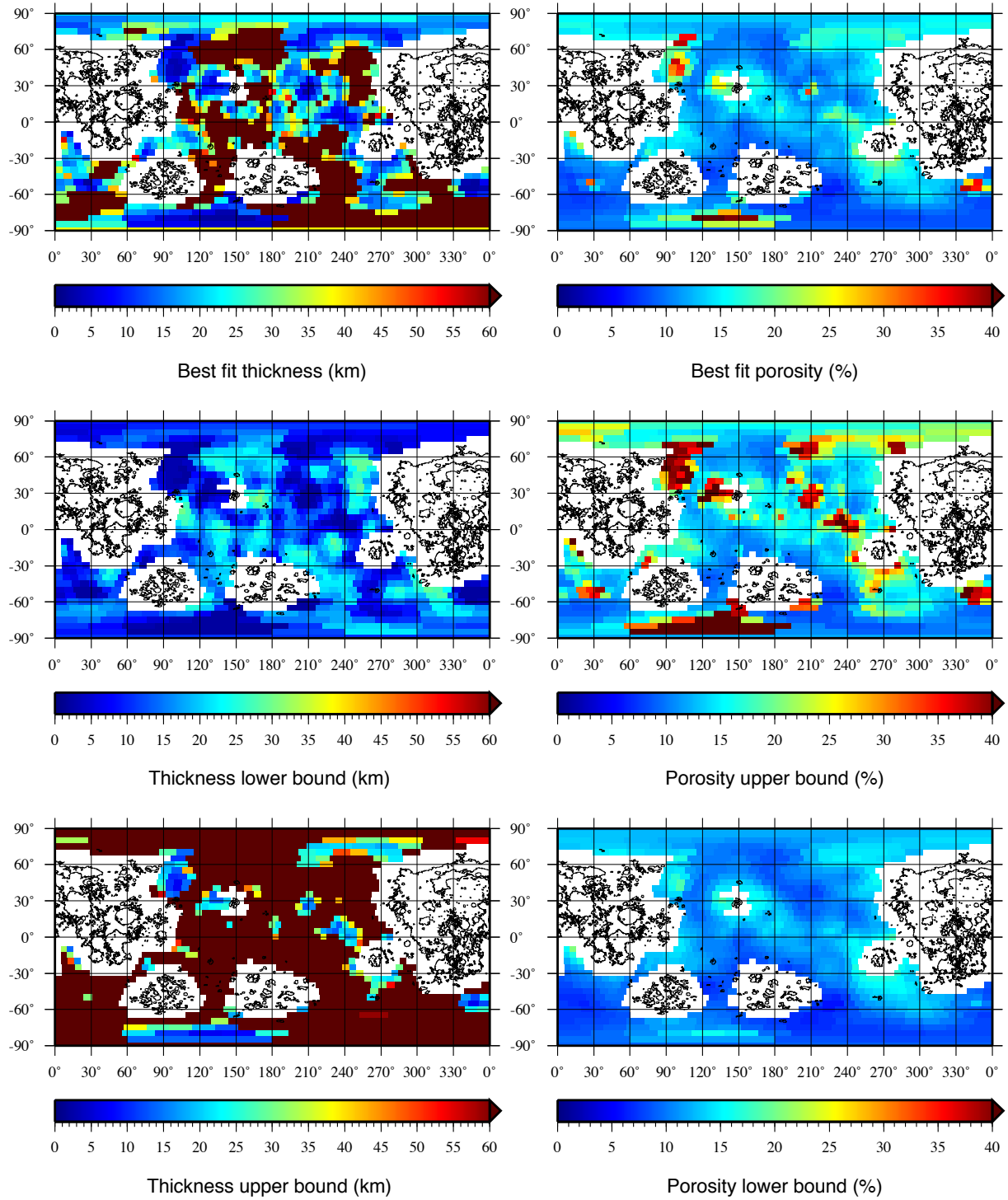


Fig. S9. Best fit layer thickness and porosity, as well as the 1- σ upper and lower bounds as determined from Monte Carlo modeling. For this analysis, localized inversions were performed using a window with 900 km diameter (corresponding to 30° of latitude).

3 Density and porosity of lunar samples

Measurements of the density and porosity of lunar feldspathic rocks, including samples collected during the Apollo program and lunar meteorites, provide a context for interpreting the results derived in this study. Twenty four feldspathic samples have been analyzed using modern techniques that contain 22-35 wt.% Al_2O_3 , corresponding to 60-95% anorthite [14,42]. The samples include a moderate abundance of mafic minerals, characterized by FeO+MgO of 0.5-18.9 wt.% and a range of magnesium numbers (the molar ratio $\text{Mg}/(\text{Mg}+\text{Fe})$) from 0.44 to 0.80. By the inclusion of lunar meteorites in the data set, it is likely to be more representative of the Moon's global crust than would be the case for measurements of Apollo samples alone [43]. The FeO abundances and Mg numbers for these samples are similar to the ranges inferred for the lunar highlands in remote sensing data [13,44]. By igneous nomenclature, these rocks are anorthosites, noritic anorthosites, and anorthositic norites, although all of these rocks have experienced considerable post-igneous processing, such as brecciation, shock melting, and sometimes thermal annealing. The measured suite of feldspathic rocks is assumed to be representative of the range of impact processing experienced by rocks in the upper few kilometers of the lunar crust.

The bulk density of the rocks is based on the total volume that includes the effects of void space from porosity. This is the density that is appropriate for use in gravity modeling. Bulk density was measured by immersion of the sample in glass beads [15], and the grain density is based on the volume of solid material in the rock, excluding the effects of porosity, as measured using helium pycnometry methods [45]. The small atomic radius of helium allows it to diffuse through even very small cracks, and it has been shown that there is no unmeasured closed pore space in these samples [14]. From the bulk and grain densities, one can calculate the porosity from eq. (13). Measurement uncertainties are typically 30-70 kg m^{-3} for the bulk density and

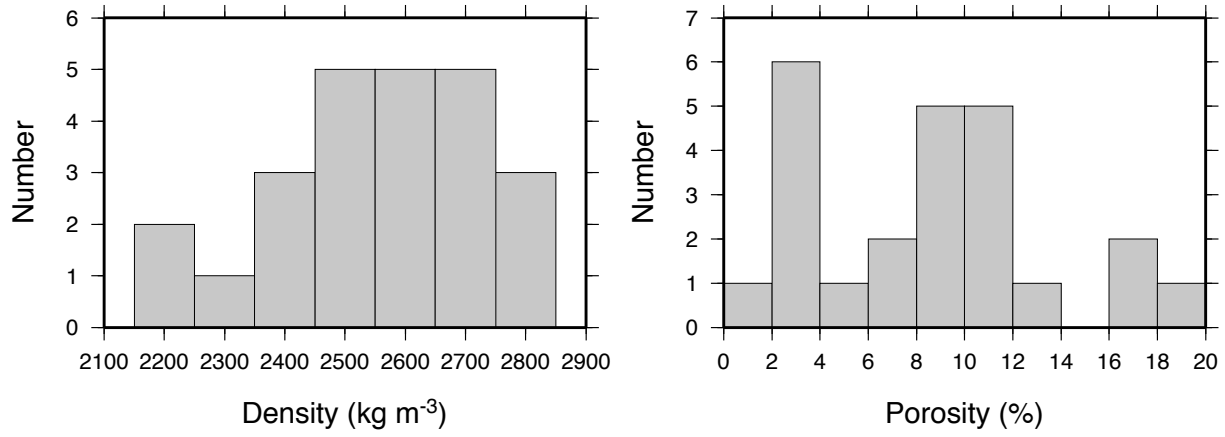


Fig. S10. Bulk density (left) and porosity (right) of twenty four feldspathic lunar rocks.

1-3% for porosity. Fig. S10 shows that the measured bulk densities have a broad, flat-topped histogram, with a mean density of $2580 \pm 170 \text{ kg m}^{-3}$, and that the porosities also have a broad distribution, with a mean of $8.6 \pm 5.3\%$.

4 Viscous closure of pore space

Rocks at elevated temperatures will flow if subjected to stress and this process can result in thermal annealing of porosity over long timescales. To calculate the time evolution of lunar porosity we follow the approach outlined in Appendix B of ref. [21]. Here, the porosity ϕ evolves according to

$$\frac{d\phi}{dt} = \phi \frac{\rho g z}{\eta} \quad (16)$$

where ρ is the crustal density, g is the acceleration due to gravity, z is depth below the surface and η is the viscosity. In general, viscosity is a function of both temperature and stress, and here we calculate η according to

$$\eta = \frac{P^{1-n}}{A} \exp\left(\frac{Q}{RT}\right) \quad (17)$$

where A and n are rheological parameters, Q is the activation energy, R is the gas constant, T is temperature, and the overburden pressure P is $\rho g z$. This approach is almost identical to that employed by ref. [46], and because of the strong temperature-dependence of viscosity, differences in the porous layer depth calculated by the two approaches are only about 1 km.

Given a temperature profile, equations (16) and (17) can be solved numerically to determine the porosity evolution as a function of time. Fig. S11 shows sets of normalized porosity profiles after 4 billions years of evolution for two different rheologies and different representative surface heat fluxes. As expected, initial near-surface porosity is unchanged because the viscosities are too high for flow to occur, while porosity at greater depth is reduced to zero. The transition interval is narrow because of the strong temperature-dependence of viscosity, and higher heat fluxes result in a thinner porous layer, as expected. Olivine (mantle) is less deformable than plagioclase (crust), and as a result, the olivine rheology has a porous layer that extends to depths that are about 15 km deeper than for crustal materials. This approach assumes implicitly that porosity is initially present and is not subsequently regenerated; such an assumption is at least

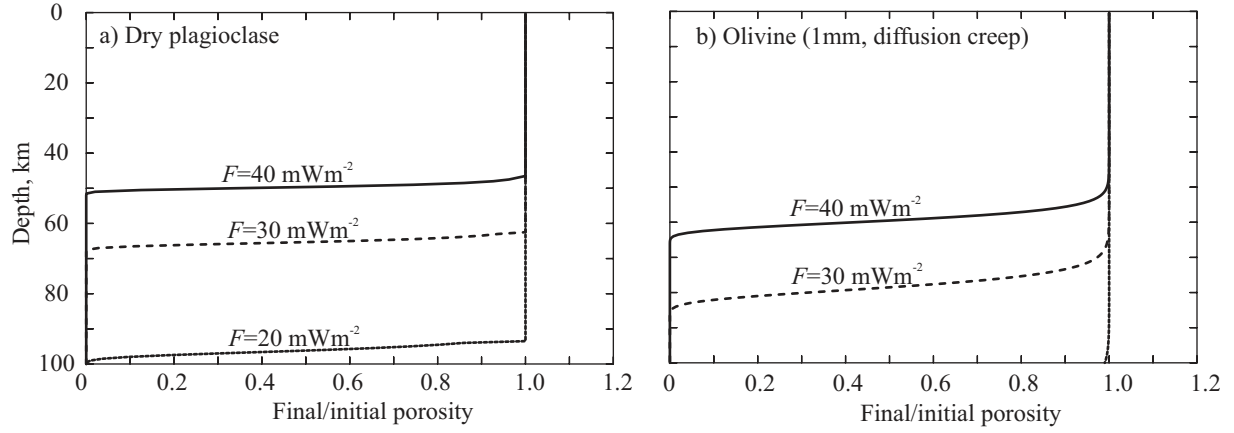


Fig. S11. Normalized porosity profiles after 4 billion years of evolution for (a) a dry plagioclase rheology and (b) a dry olivine rheology. The temperature structure is assumed constant with time and is calculated using surface heat fluxes F of 20, 30 and 40 mW m^{-2} . To produce these plots, we assumed a constant thermal conductivity of $3 \text{ W m}^{-1} \text{ K}^{-1}$, a surface temperature of 250 K, $\rho=2800 \text{ kg m}^{-3}$, and $g=1.6 \text{ m s}^{-2}$. The rheological parameters for dry plagioclase and olivine were taken from refs [47] and [48], respectively.

roughly consistent with the steeply declining impactor flux associated with the Moon.

5 Thickness of the lunar crust

We construct a global model for the thickness of the lunar crust that satisfies the observed gravity field and seismic constraints. For this model, the observed gravity is assumed to be a result of relief along the surface, relief along the crust-mantle interface (the ‘Moho’), and lateral variations in density of the crust:

$$C_{lm}^{\text{obs}} = C_{lm}^{\text{topo}} + C_{lm}^{\text{Moho}} + C_{lm}^{\rho}. \quad (18)$$

If the density of the crust depends upon position, but not depth, the first two terms can be calculated using eq. (3). For the first contribution, the surface relief is referenced to the mean planetary radius R of the Moon and possesses a density contrast $\rho(\theta, \phi)$, whereas for the second contribution, the relief of the crust-mantle interface is referenced to its mean radius D and possesses a density contrast $\rho_m - \rho(\theta, \phi)$. The gravitational contribution from lateral variations in density of the shell between the two radii R and D is calculated from the potential coefficients (referenced to radius R)

$$C_{lm}^{\rho} = \frac{4\pi R^3}{M(2l+1)(l+3)} \left(1 - (D/R)^{l+3}\right) \rho_{lm}, \quad (19)$$

where ρ_{lm} are the spherical harmonic coefficients of $\rho(\theta, \phi)$. In our model, we do not attempt to fit the total mass of the Moon (i.e., the term C_{00}), as this depends on the unknown density profile of the mantle and the size and composition of the core.

Given C^{obs} , C^{topo} , and C^{ρ} , and following ref. [26], we solve eq. (18) for the spherical harmonic coefficients of the first-order term of the Moho relief multiplied by the density contrast. The resulting non-linear equation is then solved in an iterative manner. First, given the i th estimate of the Moho relief, the spherical harmonic coefficients of the next estimate multiplied by the density contrast are calculated using

$$\left({}^{(i+1)}h\rho \right)_{lm} = \quad (20)$$

$$w_l \left[\frac{(C_{lm}^{\text{obs}} - C_{lm}^{\text{topo}} - C_{lm}^{\rho})}{4\pi D^2} M(2l+1) \left(\frac{R}{D}\right)^l - D \sum_{n=2}^N \frac{({}^{(i)}h^n \rho)_{lm}}{D^n n!} \frac{\prod_{j=1}^n (l+4-j)}{(l+3)} \right],$$

for all $l > 0$, where w_l is a filter that removes high-frequency signals resulting from physical processes not accounted for in our model (such as magmatic intrusions and lateral variations in porosity). Since we do not explicitly model the degree 0-potential coefficients, the degree-0 term of ${}^{(i+1)}h \rho$ is calculated separately as the average of ${}^{(i)}h \rho$. (If the density were constant, this term would be zero.) The function $h \rho$ is then expanded on a grid, and the relief $h(\theta, \phi)$ is obtained after dividing by the density contrast $\rho(\theta, \phi)$. To stabilize oscillations between successive iterations, and to speed convergence, the following iterative scheme is used:

$${}^{(i+3)}h = \left({}^{(i+2)}h + {}^{(i+1)}h \right) / 2, \quad (21)$$

$${}^{(i+4)}h = f \left({}^{(i+3)}h \right), \quad (22)$$

where f represents schematically the above described calculation of ${}^{(i+1)}h$. The iteration is initialized using the first-order term of eq. (20).

As an estimate for the grain density of the lunar crust, we make use of Lunar Prospector elemental abundances and an empirical correlation between grain density and composition (see section 1). Given that the most prominent lateral variations in density are associated with broad compositions units, such as the highlands and South Pole-Aitken basin, we use the 5° gridded Lunar Prospector data of ref. [13]. The crust beneath the mare basalts is thought to be broadly anorthositic in composition, and we discard all pixels that contain any such deposits, as well as a few pixels that yield grain densities larger than about 3050 kg m^{-3} . A global grid for the crustal grain density is then obtained by interpolating among the remaining data (Fig. S12). The average grain density of the crust is 2927 kg m^{-3} , and the bulk density is obtained by multiplying each pixel in this map by $(1 - \phi)$.

To obtain a unique crustal thickness model, we vary the average thickness of the crust ($R - D$) and the mantle density ρ_m in order to find a solution that fits the seismic constraints at the

Apollo 12 and 14 sites and that has a minimum crustal thickness less than 1 km. The mantle density that is obtained should be considered as being representative only to the minimum radius of the crust-mantle interface, which is less than 80 km below the surface: below this depth, there is no gravitational signature in our model associated with relief along the crust-mantle interface and the mantle density is entirely unconstrained. The degree $\lambda_{1/2}$ at which the filter w_l achieves a value of 0.5 was chosen to be close to 80 in order to minimize high frequency signals that are not accounted for in our model, and that would otherwise be mapped into crustal thickness variations. Furthermore, to avoid noise in the gravity field, the gravity coefficients were truncated above degree 310. All calculations were performed using $N = 7$, and to avoid aliases when computing the spherical harmonic coefficients of ρh^n , grids that resolve signals up to spherical harmonic degree 930 were used [49].

Tests show that if lateral variations in crustal density were neglected, long wavelength errors with amplitudes of ± 4 km would arise. In particular, by including lateral variations in density, the thickness of the crust within the South Pole-Aiken basin is about 4 km thicker, and the thickest portion of the farside highlands crust is about 4 km thinner, than would be obtained from a uniform density model. Crustal models constructed using the GRAIL bulk density maps (Fig. 1) give nearly identical average crustal thicknesses as those derived using the grain density map of Fig. S12 and yield lateral variations in thickness that are very similar to those of Fig. 3. Since we do not yet have good constraints on how crustal porosity varies with depth in both the crust and mantle, using the GRAIL bulk densities for the entire crust is not justified at the present time. The neglect of the gravitational signal arising from the dense mare basalts should have only minor consequences on our crustal thickness model. The mare basalts are in general less than 1 km thick [11], and with a density close to that of the mantle, the neglect of the these deposits would only bias the thickness of the crust downward by an amount equal to the thickness of these deposits.

Analyses of the Apollo seismic data initially suggested that the crust was about 60 km thick in the region of the Apollo 12 and 14 landing sites [50], and this value was used as a constraint in several global crustal thickness models following the Clementine mission [26,51,52]. After the Lunar Prospector mission, reanalyses of the Apollo seismic data by two groups showed that the crust was significantly thinner in this region than once thought. Ref. [53] initially suggested a thickness of 45 ± 5 km in the Apollo zone, which was later revised to 38 ± 3 km [24]. An independent analysis by ref. [22] obtained a value of 30 ± 2.5 km, with a later analysis suggesting values of 33 ± 5 and 31 ± 7 km for the Apollo 12 and 14 landing sites [54], respectively. Most subsequent crustal thickness models were not able to fit the revised seismic and minimum crustal thickness constraints, and in retrospect, this was because these studies employed a crustal density between 2800 and 2900 kg m⁻³ that is appropriate for the grain density, but not the bulk density when porosity is considered. Because of this, along with initial skepticism to the revised seismic estimates, most subsequent studies [11,27,55] either employed the 45 km constraint of ref. [53] or ignored the Apollo seismic data altogether. Ref. [54] was successful in reconciling the seismic and crustal thickness modeling, but their study did not consider crustal densities below 2600 kg m⁻³, and was based on Lunar Prospector-based gravity models that possessed poor resolution over the far side hemisphere.

Several crustal thickness models are summarized in Table S1. The two pre-GRAIL models predict an average crustal thickness of 53 km [11,27] and crustal thicknesses near 45 km at the Apollo 12 and 14 landing sites. Using the grain density map of Fig. S12 with a 12% porosity, and using a 30-km seismic constraint at the Apollo 12 and 14 sites, the average crustal thickness and mantle density are predicted to be 34 km and 3220 kg m⁻³, respectively. For an assumed porosity of 7%, the average crustal thickness barely changes, but the mantle density increases to 3360 kg m⁻³. This behavior is easily understood: the largest crustal thickness variations are a result of relief along the crust-mantle interface, and not surface topography, and the amplitude

of this relief is controlled by the density contrast between the crust and mantle. A change in crustal density simply trades off to a change in mantle density. Using a seismic constraint of 38 km at the Apollo 12 and 14 sites, the average crustal thickness increases to 43 km, and the mantle density decreases by about 60 kg m^{-3} . For these models, the degree where the filter w_l is 0.5 was reduced to 70 in order to attenuate the amplification of high-frequency signals that occurs when evaluating the gravity field at a deeper crust-mantle interface.

A final crustal thickness model was constructed under the assumption that porosity exists in a layer of constant thickness confined between the surface and depth z . Mathematically, the porosity in this layer is modeled as having a density $-\phi \rho_c(\theta, \phi)$, and the gravitational contribution from this void space is added to the other contributions in eq. (18). A gravity signal is generated with a density contrast $-\phi \rho_c(\theta, \phi)$ at the surface, and also from an equal an opposite density contrast $\phi \rho_c(\theta, \phi)$ with the same relief, but z km below the surface. The density contrast should in fact be $-\phi \rho_m$ wherever the crust is thinner than z , but since this only occurs beneath giant impact basins where temperatures could have exceeded the solidus, it is reasonable to use a density contrast with a smaller amplitude in these regions. As with our previous models, the largest variations in crustal thickness are a result of relief along the crust-mantle interface, and not relief along the surface. With the porosity contribution already having been accounted for, the density contrast at the base of the crust is $\rho_m - \rho_c(\theta, \phi)$, which is smaller by $\phi \rho_c$ than those used in our previous models. This density contrast is similar to that used in the pre-GRAIL models, and it is not possible to construct a global crustal thickness model that satisfies both the Apollo seismic and minimum crustal thickness constraints, regardless of the values chosen for ϕ and z . If the seismic constraint is ignored, and if the mantle density is set to 3400 kg m^{-3} to maximize the density contrast, an average crustal thickness of $\sim 65 \text{ km}$ is obtained, with a thickness close to $\sim 57 \text{ km}$ at the Apollo 12 and 14 sites.

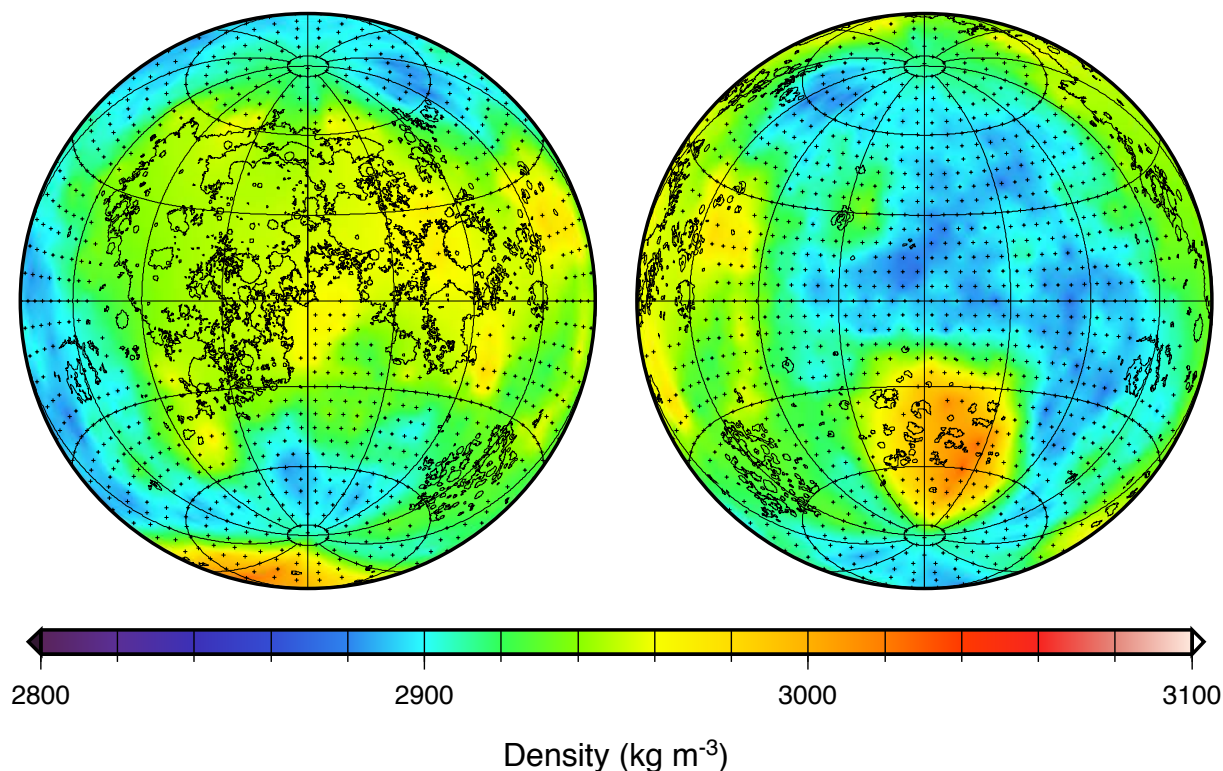


Fig. S12. Grain density of the lunar crust used for constructing a global crustal thickness model. Grain densities exterior to the mare (indicated by the symbol +) were estimated from the 5° Lunar Prospector compositional data along with an empirical correlation between composition and density. After discarding a few pixels with densities greater than about 3050 kg m⁻³, a global map was determined by interpolating among the remaining data. Image format the same as Fig. S3.

Table S1. Summary of crustal thickness models. Those models that include crustal porosity make use of the crustal grain density map in Fig. S12.

Model	Average thickness, km	Minimum thickness, km	Apollo 12/14 thickness, km	ρ_c or ϕ	ρ_m , kg m ⁻³	$\lambda_{1/2}$
Lunar Prospector gravity, Clementine topography						
<i>Wieczorek et al. (2006)</i>	53.4	0	45	2900 kg m ⁻³	3320	30
Kaguya gravity and topography						
<i>Ishihara et al. (2009)</i>	53	1.2	47.5	2800 kg m ⁻³	3360	50
GRAIL gravity and LRO topography						
<i>Model 1</i>	34	0.6	29.9	12%	3220	80
<i>Model 2</i>	35	0.2	30.8	7%	3360	80
<i>Model 3</i>	43	1.0	38.1	12%	3150	70
<i>Model 4</i>	43	0.5	38.0	7%	3300	70